First-principles study of solute strengthening of twinning dislocations in Mg alloys

M. Ghazisaeidi

Department of Materials Science and Engineering,

Ohio State University, Columbus, Ohio,43210, USA

L. G. Hector Jr

General Motors Global R & D, Warren, MI 48090-9055, USA

W. A. Curtin

Institute of Mechanical Engineering,

École Polytechnique Fédérale de Lausanne, Lausanne CH-1015, Switzerland

Abstract

Solute strengthening of twin dislocation motion along an existing twin boundary in Mg-X (X=Al, Zn) is investigated using a new Labusch-type weak pinning model. First, the $(10\bar{1}2)$ twinning dislocation structure is computed using first-principles methods. Second, the interaction energies of Al and Zn solutes with the twin boundary and twin dislocation are computed. Interaction energies are computed for all solute positions for Al and a subset of sites for Zn, and it is shown that the interaction energies of Zn solutes scale with the Al solute energies in propotion to the misfit volume plus an additional "chemical" interaction piece and this scaling is used to compute the Zn solute interactions at all other sites around the twin dislocation. Third, the solute/dislocation interaction energies are used in a new Labusch-type model to predict the overall solute strengthening of the twinning dislocation. New features emerge in the application of the model to twinning because of the very small Burgers vector of the twin dislocation, leading to a new functional form for the dependence of the strengthening on concentration, temperature, and strain rate. Fourth, application of the model leads to parameter-free predictions that agree well with available experimental data on various Mg-Al-Zn alloys. The predicted strengthening is not large, e.g. ≈ 10 MPa for the AZ31 alloy at room temperature, but is larger than the strengthening of basal slip by the same solutes. Overall, this work contributes to a growing quantitative understanding of alloying effects on various deformation modes in Mg.

I. INTRODUCTION

The high strength-to-weight ratio of magnesium alloys makes them good candidates for lightweight structural metals. The automotive industry, in particular, has been focused on potential applications of wrought magnesium alloys to achieve lighter-weight, more fuel-efficient vehicles. However, limited room temperature formability has prohibited the widespread use of Mg alloys. This limitation is caused by the anisotropic plastic response due to the underlying hexagonal closed packed (hcp) structure; the stress required to operate basal slip is much lower than that for non-basal (pyramidal and prism) slip and somewhat less than that for twinning. The von Mises criterion for strain compatibility requires the operation of at least five independent systems (slip and twinning), and these are not available at low temperatures due to the very high stresses needed to operate non-basal modes; fracture thus precedes significant plastic deformation, resulting in low ductility. The addition of alloying elements capable of modifying the strengths of various deformation modes holds promise as a means to promote non-basal deformation modes and, in principle, reduce the critical stress differential between basal and non-basal deformation modes to increase ductility at moderate temperatures.

Recent computational work, based on first-principles calculations, has begun to establish a quantitative, theoretical basis to predict the effects of solutes on basal slip[1, 2] and the thermally activated basal to prism cross slip behavior in Mg[3, 4]. Despite great advancements, a quantitative study of solute effects on major non-basal deformation modes ($\langle c+a \rangle$ slip and twinning) does not exist yet. In this paper, we use first-principles methods to compute the twin dislocation structure and the twin dislocation/solute interaction energies for Al and Zn solutes. We then use these energies to predict the effects of these solutes on the finite-temperature, finite-strain-rate strengthening of $(10\bar{1}2)$ twinning, which is the only active deformation mode in c-axis tension of single crystals and is the most dominant twin mode in Mg[5]. The models predict that, at room temperature, alloying shows a significant strengthening effect on the twin dislocation glide in comparison to the strengthening of basal slip. The stresses resisting twin growth are not large ($\approx$ 10 MPa) but are larger than the "Peierls barrier" in pure Mg ($\approx$ 3 MPa), and so make a distinct contribution. However, the strengthening must be compared to stress levels required for twin nucleation, which may be controlled by other defects or dislocation interactions; this issue is beyond the scope of the

present paper. The rest of this paper is organized as follows. In Section II, we present the computational methods and the computed twinning dislocation structure and interaction energies with solutes. In Section III we present the strengthening model and its application to the present problem involving the tension twin dislocation. In Section IV, we show the predictions of the model, compare with experiments, and draw implications from the model. We summarize this work in Section V.

II. TWINNING DISLOCATION STRUCTURE AND INTERACTION WITH SOLUTES

We use density functional theory (DFT) to study the structure of the Mg $(10\bar{1}2)$ twin boundary, the corresponding twinning dislocation, and the twin/solute interaction energies for Al and Zn substitutional solutes. The DFT calculations are performed with the VASP code [6, 7], a plane-wave based density functional theory code using Vanderbilt-type ultrasoft pseudopotentials and the generalized-gradient approximation[8] for the exchange-correlation potential. The 3s states of Mg are treated as valence electrons. A plane-wave energy cut-off of 138 eV is used throughout the calculations with pure Mg. The cut-off energy is increased to 169 eV and 272 eV in calculations involving Al and Zn respectively. A $16 \times 16 \times 12$ k-point mesh with Methfessel-Paxton smearing of 0.5 eV is used for a Mg unit cell and is adjusted for the supercells accordingly.

We start with the coherent twin boundary structure. The initial geometry is constructed by applying a mirror symmetry operation to the perfect Mg lattice on the $(10\bar{1}2)$ plane. Two twin boundaries with a separation of 14 atomic layers are created and periodic boundary conditions are applied in all directions. This corresponds to a $7.58\mathring{A} \times 3.19\mathring{A} \times 54.20\mathring{A}$ supercell with 56 atoms. All atomic positions and the supercell dimension perpendicular to the boundary are allowed to relax until the forces are smaller than 5 meV/Å. We compute a twin boundary energy of 114 mJ/m^2. For solute/twin-boundary interaction energies, the dimensions of the supercell are doubled along the directions in the twin boundary plane to avoid nearest-neighbor interactions between a solute atom and its periodic images. Our reference configuration is taken to be a system with one solute atom at a bulk-equivalent site (half way between the two twin boundaries in the supercell. Eight unique solute sites in and near the twin boundary are identified and numbered according to their distance from the

twin boundary, as shown in Figure 1. The solute/twin-boundary interaction energy at each site is then defined by the difference between the energy of the system with a solute atom at that site and the reference energy at the bulk-equivalent site. The interaction energies are shown in Figure 1a. With increasing distance from the boundary, the interaction energy reduces rapidly to zero. Table I shows the numerical values of the interaction energies at the selected sites for the Al and Zn solutes. These calculation are similar to those reported in [9] for interaction of Zn and Gd with Mg $(10\bar{1}2)$ twin boundary; the Zn interaction energies in that work are consistent with the present work. The solute misfit volume Δv is calculated with DFT following the method described in [10] and we find Δv -8.22 $\mathring{A}^3$ and -10.65 $\mathring{A}^3$ for Al and Zn solutes respectively. The solute/twin interaction energies in the twin boundary generally scale with the solute misfit volumes, due to the positive and negative pressures in the two different atomic sites in the twin, respectively.

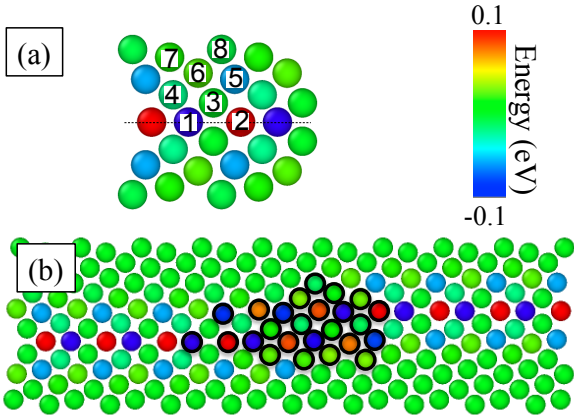

FIG. 1: Twin/solute interaction energy map for Al solutes: (a) energies at geometrically unique sites in and around the coherent twin boundary, labelled based on their distance from the twin boundary for later use; note that the strongest interactions occur at the twin boundary with opposite signs (attractive and repulsive); (b) twin dislocation structure and the solute interaction energies computed by direct substitution of Al atoms at sites in the twinning dislocation core as indicated by sites outlined in bold.

The twinning dislocation (disconnection) is a line defect with both dislocation and step characters [11–13]. In the case of $(10\bar{1}2)$ twin, the twinning dislocation step involves two atomic planes. As the twinning dislocation glides on the twin plane, it transforms the crystal structure on one side to the corresponding mirror structure, advancing the twin boundary by

TABLE I: Twin/solute interaction energies (eV) for Al and Zn solutes placed near the twin boundary. Site numbers are explained in Figure 1a.

Site	Al	Zn
1	-0.150	-0.220
2	+0.105	+0.080
3	-0.002	-0.029
4	-0.023	-0.045
5	-0.058	-0.092
6	+0.020	+0.026
7	+0.009	+0.004
8	-0.008	-0.008

the step height. The Burger's vector character of the twinning dislocation is geometrically related to the twinning shear and is defined as a fraction of the perfect lattice vector along the twinning shear direction as

$$\vec{b}_t = s[10\bar{1}\bar{1}]$$

where $s = 0.064$ is determined by the shear necessary to create a two-layer-thick twin lamella and is computed using the DFT-computed c/a ratio of 1.623 for Mg [14]. The twinning dislocation in the simulation cell is constructed following the procedure given in Appendix A. The simulation cell contains 858 atoms embedded in a surrounding vacuum, with the ions within 10 Å of the outer boundaries being held fixed. Periodicity along the dislocation line is used with a repeat distance of a_0. This structure is then relaxed using the DFT-derived ionic forces while fixing the atomic positions near the edges of the simulation cell. Such a large fixed cell is viable for the twin dislocation because of the very small burgers vector, and compact structure, which together minimize spurious interactions with the outer cell boundary. The final predicted dislocation geometry is shown in Figure 1b, and consists of a compact core around the step while maintaining two well-defined twin boundaries away from the step. The atomic coordinates in the relaxed twinning dislocation geometry are provided in the supplementary materials. The DFT-predicted structure of the Mg tension

twin dislocation is the first main result of this paper.

The relaxed twinning dislocation geometry is used to directly compute the Al solute/twin-dislocation interaction energies. The periodic dimension along the dislocation line is doubled for the solute calculations. On the other hand, since the defect core is compact, we use smaller dimensions in the other two dimensions, resulting in a super cell containing 1271 Mg and 1 Al atom. Figure 1b shows the twinning dislocation/solute interaction energy map for a single Al atom placed at each of the various sites around the dislocation core indicated by the bold outlines. The solute/twin-dislocation interaction energies in the core are generally less than the solute/twin-boundary interaction energies, so that the twin boundary dominates the energetics in this problem. Outside the dislocation core where DFT energies have been computed, the interaction energy can be approximated by the sum of the solute/twin-boundary interaction energy (Table I) plus an elastic interaction energy $-p(x_i, y_j)\Delta v$ due to the interaction of the dislocation pressure field $p(x_i, y_j)$ and the solute misfit volume Δv, as shown in Figure 1b. The pressure field is calculated using the continuum expression $p(x_i, y_j) = -\frac{1+\nu}{3\pi(1-\nu)}\mu b\frac{y_i}{x_i^2+y_j^2}$ for a point dislocation; since the Burger's vector is very small, we do not spread the core as in the Peierls-Nabarro model and the contribution due to the pressure field is small. In general, placing the solute near the twin dislocation core of the does not have a strong effects on the defect core structure[1]. We have also computed the solute/dislocation interaction energies for Zn solutes at selected sites around the twin dislocation core. The results are shown in Figure 2a where the DFT results are indicated by the bold-outlined sites. The determination of solute/twin-dislocation interaction energies by DFT is the second main result of this paper.

Because direct DFT calculations of the solute/twin-dislocation interaction energy are computationally very expensive, we now describe and validate a computationally-tractable

[1] The exception is for a solute at site 5 in the core immediately ahead of the dislocation, for which the system lowers its energy by displacing the atoms around the solute so that site 5 (with respect to the left twin boundary) becomes a site 1 in the right twin boundary (note the dark blue sites in the core region shown in Figure 1b). This migration is driven by the large energy difference between sites 5 and 1 (-0.092). To compute an interaction energy at this site, we therefore place two Al atoms at equivalent site 5 positions relative to the core, one on each twin boundary, which exert equal and opposite forces on the twin dislocation and prevent migration. The twin-dislocation/solute interaction energies at these two sites should be equal, and so the site 5 energy is one-half of the computed energy and is the value shown in the figure; the interaction energy at this site is higher than that at site 1 in the coherent boundary by 0.034 eV and lower than that of site 5 in the coherent boundary by -0.059 eV.

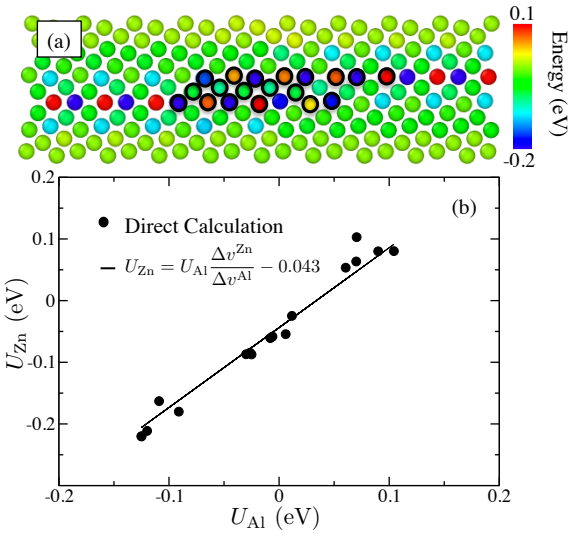

FIG. 2: Zn/Twin interaction energies. (a) interaction energies are calculated with DFT at selected sites indicated by bold-outlined circles. The energies are obtained by scaling Al interaction energies at the remaining sites. (b) DFT-computed solute/twin-dislocation interaction energies for Zn versus the energies computed for Al at the same atomic sites; solid line demonstrates the validity of the scaling relation of Equation 1 based on solute misfit volumes plus a small "chemical" interaction.

method to accurately estimate the interaction energies without full DFT calculations using the twin core and considering all possible sites around the core; this method can then be used for many other solutes in future work. We propose that the interaction energies are proportional to the solute misfit volume plus a (small) "chemical" contribution specific to the solute. In other words, for a solute of type i, we postulate that $U_i(x,y) = A\Delta v_i + B_i$ where A is a function of the matrix material only. Then, given the interaction energies $U_{Al}(x,y)$ for Al, we can express the interaction energies for any other solute as

$$U_i(x,y) = U_{Al}(x,y)\Delta v_i/\Delta v_{Al} + \Delta B_i \tag{1}$$

where $\Delta B_i = B_i - B_{Al}\Delta v_i/\Delta v_j$.

Operationally, we simply take ΔB_i as a fitting parameter. To validate Equation 1, we compare our direct DFT results for Zn to the values predicted by using the DFT results for Al scaled according to Equation 1. The results are shown in Figure 2b, and the agreement is very good over a wide range of Zn/twin interaction energies with the "chemical" contribution of $\Delta B_{Zn} \approx$ -0.043 (eV). Note that inclusion of the "chemical correction" introduces an error

away from the twin in the bulk material and so should only be used inside the core and close to the twin boundary. Using this validated scaling relation, we can now obtain the Zn/twin interaction energies at sites not computed via direct DFT, and we apply these scaled energies at sites within a vertical distances of $5\mathring{A}$ from the center of the twinning dislocation. The elastic interaction energy of $-p(x_i, y_j)\Delta v^{\mathrm{Zn}}$ is used for further sites, thus recovering the proper bulk limit. The overall computed energies for Zn solutes around the dislocation core are shown in Figure 2a. We note that the scaling method allows calculation of interaction energies for arbitrary solutes from the direct Al interaction energies using simple DFT calculations of misfit volumes and solute/twin boundary interaction energies (e.g. as shown in Table I) to determine the "chemical" contribution. This new strategy is the third main result of this paper.

III. SOLUTE STRENGTHENING MODEL

Strengthening models for substitutional solutes are broadly divided into two classes: strong pinning (Friedel) where individual solutes act as point obstacles to dislocation motion and weak pinning (Labusch) where collective interaction of many solutes with the dislocation results in strengthening in regions of favorable statistical fluctuations in the solute configuration. Each model has characteristic scalings with solute concentration and temperature. However, Ref [15] shows that the energy barriers for the Friedel model are those of the individual solutes, and the solute interaction energies shown above are easily overcome at finite temperatures so that no strengthening is predicted above ≈ 100 K. Here, we thus use only a new Labusch-type model[16], which has been shown to be predictive for strengthening in fcc Al and basal slip in Mg, to quantify the solid solution strengthening on twin growth. The weak pinning Labusch-type model is based on the collective effect of solutes rather than individual solute/dislocation interactions [17]. A straight dislocation bows out in the glide plane towards favorable environments of the random solute distribution to minimize the potential energy. However, bowing has a cost in elastic energy. Therefore, the favorable configuration of a dislocation is that which minimizes the total energy as a function of the dislocation bowing segments of length ζ and the amplitude of the bowing w. In the new quantitative and predictive Labusch-type model introduced by Leyson *et al.*[16], the characteristic segment length ζ_c and amplitude w_c are obtained by minimizing the total energy

of the fluctuating dislocation line with respect to both ζ and w.

In the model, the total energy (potential+elastic) as a function of roughening amplitude w and segment length ζ is given by

$$E_{tot}(\zeta, w) = \left[\left(\Gamma\frac{w^2}{2\zeta}\right) - \left(\frac{c\zeta}{a_0}\right)^{1/2}\Delta\tilde{E}_p(w)\right]\frac{L}{2\zeta} \tag{2}$$

where L and a_0 are line length and periodicity along the line direction (lattice parameter) respectively and Γ is the dislocation line tension. We approximate the line tension as $\gamma = 0.040\ eV/\mathring{A}$, consistent with the defect core energy (dominated by the step) calculated using the EAM Liu potential[18], which predicts the twin boundary and twinning dislocation geometry in good agreement with DFT[19]. The quantity $\Delta\tilde{E}_p(w)$ is given by

$$\Delta\tilde{E}_p(w) = \left[\sum_{ij}\left(U(x_i, y_j) - U(x_i - w, y_j)\right)^2\right]^{1/2} \tag{3}$$

with $U(x_i, y_j)$ being the solute/dislocation interaction energy for a solute at position (x_i, y_j) in the plane perpendicular to the dislocation line and relative to a dislocation at the origin $(x = 0, y = 0)$. Minimizing the total energy with respect to ζ gives a characteristic segment length ζ_c as a function of w and the total energy at this characteristic segment length as a function of w only. The characteristic roughening w_c is then obtained by numerical minimization of E_{tot}/L. From this mininum energy, the energy barrier ΔE_b and the zero temperature yield stress τ_{y0}^L controlling motion of the segments of length ζ_c can be expressed in terms of the characteristic material parameters as

$$\Delta E_b = \alpha\left(\frac{\Gamma w_c^2\Delta\tilde{E}_p^2(w_c)c}{a_0}\right)^{1/3} \tag{4}$$

and

$$\tau_{y0} = \beta\left(\frac{c^2\Delta\tilde{E}_p^4(w_c)}{\Gamma a_0^2 w_c^5}\right)^{1/3} \tag{5}$$

where the prefactors α and β in Equation 4 and Equation 5 contain all the numerical coefficients determined by the geometry of the lattice and the specific slip systems, and for the twin dislocation in Mg are $\alpha = (4\sqrt{2} - 1)/2^{5/3}$ and $\beta = \frac{\pi}{2b}(4\sqrt{2} - 1)/2^{7/3}$. The finite temperature, finite strain rate flow stress follows again from standard thermal activation theory. The stress-dependent energy barrier takes the form

$$\Delta E^(\tau) = \Delta E_b\left[1 - \left(\frac{\tau}{\tau_{y0}^L}\right)\right]^{3/2}. \tag{6}$$

In general, at sufficiently high temperatures relative to the energy barrier (and corresponding to low applied stresses), the energy barrier can have additional contributions from long-range solute/dislocation interactions [20]. Since the interaction energy here is dominated by solutes in the core (the far-field interaction due to the pressure field is small because the burgers vector is small), these additional contributions are negligible for the twin dislocation in Mg and are thus neglected here. The finite temperature yield stress τ_y is expressed as

$$\tau_y^(T,\dot{\epsilon}) = \tau_{y0}\left[1 - \left(\frac{T}{T_0}\right)^{2/3}\right] \tag{7}$$

where $T_0 = \Delta E_b/(k_B \ln(\dot{\epsilon}/\dot{\epsilon_0}))$ is the characteristic temperature for the Labusch mechanism.

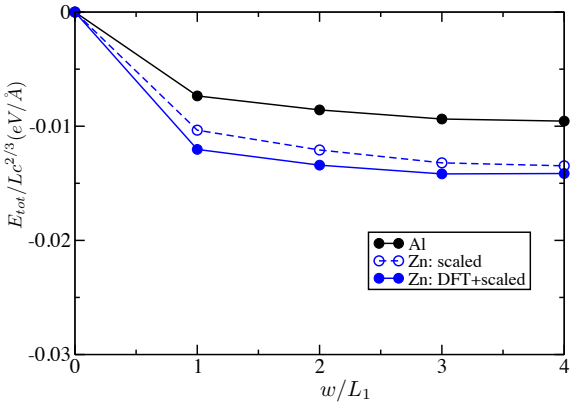

FIG. 3: Normalized energy per unit length vs. roughening amplitude normalized by the periodicity of the coherent twin boundary $L_1 = 7.58\mathring{A}$ for Al and Zn solutes interacting with twinning dislocation in Mg. The Zn interaction energies are obtained by direct DFT calculations at selected sites and scaling Al interaction energies elsewhere. Use of the scaled energies everywhere introduces an error of ≈ 0.001 meV/Å in the normalized total energy.

Using the solute/twin dislocation interaction energies obtained from DFT and dislocation pressure field, we compute the total energy per unit length of dislocation $E_{tot}(w)/L$ for various values of the roughening amplitude w as shown in Figure 3. Unlike in the previous applications to fcc Al and basal slip in Mg, a clear minimum in the total energy *does not emerge* from the analysis; this is unique to the twin because the interaction energies are dominated by the solute/twin-boundary energies rather than the solute/dislocation energies. In the Mg twin, the interaction energy is nearly periodic with respect to the twin periodicity L_1 so that $U(x_i + nL_1, y_j) = U(x_i, y_j)$ for any integer n multiple of L_1. Therefore, except

around the core where a change in periodicity occurs, various roughening amplitudes, given by multiples of L_1, have nearly equal contributions to $\Delta\tilde{E}_p(w)$ and thus affect the total energy by comparable amounts. The existence of multiple roughening amplitudes of nearly identical energy distinguishes the weak pinning of twinning dislocation from that of lattice dislocations, which have well-defined w_c values. The analysis of strengthening for the twin dislocation is thus more complex than outlined above. For fixed values of temperature, concentration, and strain rate, there are now many possible configurations available for the twinning dislocation to optimize its energy. i.e. the dislocation line may bow out by multiples of L_1 towards favorable solute distributions. Among all of these configurations, the one requiring the highest stress to achieve the desired strain rate at any given temperature is the configuration that controls the strengthening. Thus, a prediction of the yield stress versus temperature and concentration requires calculation of the strength for all possible roughening amplitudes w and then a determination of the maximum strength among all these strength values. The strength versus temperature at a given c and strain rate is then constructed as the "envelope" of the strength vs. T curves for each integer $w = nL_1$. Creation of the envelope is straightforward but unwieldy. Since $E_{tot}/(Lc^{2/3})$ is essentially constant for all the integer values of $w = nL_1$ (see Figure 3), we can develop an analytic model by considering w as a continuous variable for $w \geq L_1$, and carrying out the maximization analytically. Such an analysis is presented in detail in the Appendix B; here we present the final result for the finite-T, finite strain-rate yield stress as (for $w \geq L_1$)

$$\tau_y(T,\dot{\epsilon}) = \frac{2\pi(33-8\sqrt{2})}{25\sqrt{5}b}\frac{[-E_{tot}/Lc^{2/3}]^{3/2}\sqrt{\Gamma}c}{k_BT\ln\dot{\epsilon}_0/\dot{\epsilon}} \tag{8}$$

where $E_{tot}/(Lc^{2/3})$) is the computed constant value for $w \geq L_1$ shown in Figure 3 for the given solute. Moreover, this model can be generalized to alloys with multiple solutes (see Appendix B) as

$$\tau_y(T,\dot{\epsilon}) = \frac{2\pi(33-8\sqrt{2})}{25\sqrt{5}b}\frac{\sqrt{\Gamma}\sum_i c_i[-E_{tot}/Lc^{2/3}]^{(i)3/2}}{K_bT\ln\dot{\epsilon}_0/\dot{\epsilon}} \tag{9}$$

where i ranges over the number of alloying elements. As an example, Figure 4 shows the predicted numerical yield stress envelope (discrete integer values of w from $n = 1-4$ only are shown) as a function of temperature for 1 at.% Al along with the analytical model (continuous w). The two predictions are in excellent agreement. The differences at low T are simply due to using w as a continuous variable below $w = L_1$; other differences reflect

the fact that $E_{tot}/(Lc^{2/3}))$ is not perfectly constant as a function of w for $w > L_1$. At low temperatures (near $T = 0K$), the roughening amplitude $w = L_1$ controls the strengthening. At $T \approx 27K$, $w = 2L_1$ becomes the controlling roughening amplitude, and transitions to larger roughening amplitudes continue as T increases. The abrupt changes in slope in the discrete model are artifacts of the restriction that only one single amplitude is relevant at any one temperature. As T increases, the dislocation can roughen to larger and larger amplitudes and therefore there is always some w that will give a finite (although perhaps very small) yield stress, and this is embedded in the analytical stress envelope. In addition, the analytical relation for the yield stress allows for quantifying the sensitivity of the predictions to the value of $E_{tot}/(Lc^{2/3})$ value. For instance, Figure 3 shows that using the scaled energy values for Zn solutes at all sites around the core instead of a mixture of direct DFT+ scaled energies introduces a change of ≈ 0.001 meV/$\mathring{A}$ in $E_{tot}/(Lc^{2/3}))$ which introduces an error of $\approx 10\%$ in final τ_y predictions. The new model of Equation 8 for solute strengthening of the twin dislocation in Mg is the fourth main result of this paper.

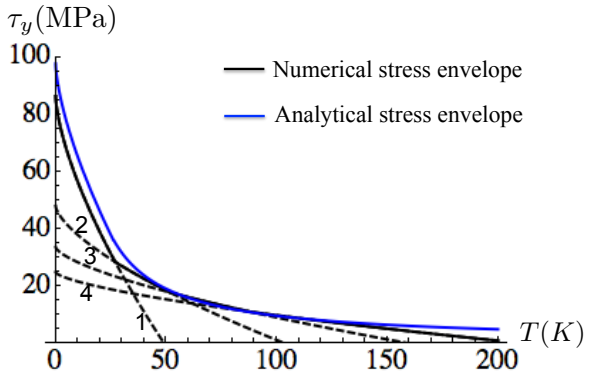

FIG. 4: Yield stress versus temperature for 1at.% Al concentration as predicted as the upper envelope (solid line) among the strengths for successive discrete roughening amplitudes $w = nL_1$ (dashed lines, only n = 1-4 shown) and as predicted by the continuous analytical model of Equation 8 (blue line). Agreement between the discrete and continuous analytic models is excellent.

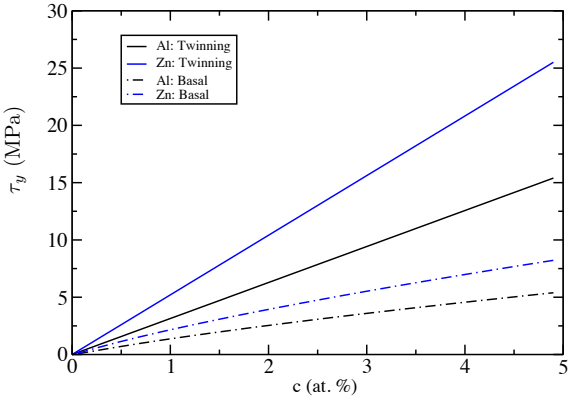

FIG. 5: Yield stress for twin dislocation motion τ_y at T=300 K as a function of solute concentration for Al and Zn solutes. The yield stress for basal slip is shown for comparison (Al results in [2]; Zn results unpublished).

IV. PREDICTIONS FOR Mg ALLOYS AND COMPARISONS WITH EXPERIMENTS

Figure 5 shows the predicted yield stress τ_y at T=300 K due to solute strengthening as a function of solute concentration for Al and Zn solutes. In these predictions, we use a reference strain rate of $\dot{\gamma} = 10^5/s$ and values of $E_{tot}/(Lc^{2/3})) = -0.009$ meV/$\mathring{A}$ for Al and -0.014 meV/$\mathring{A}$ for Zn, corresponding to the average values shown in Figure 3. Also shown for reference are the predictions of strengthening of basal slip from earlier applications of the Labusch-type model [2]. We predict that Al and Zn strengthen twinning more strongly than basal slip, and therefore promote anisotropy in the plastic deformation modes. In addition, the twinning yield stress scales linearly with solute concentration c, which is stronger than the nominal $c^{2/3}$ dependence for basal strengthening [2]. This difference is due to the fact that the roughening amplitude for the twinning dislocation can vary because the burgers vector is very small, and consequently the line tension Γ is an order of magnitude smaller for the twinning dislocation compared to the basal dislocation, and the strengthening is controlled mainly by the solute/twin-boundary interactions; all these features lead to a critical w_c that depends on concentration as $c^{-1/3}$ (see Equation B5). The different physical behavior also leads to scalings with concentration, temperature, and strain rate that differ from those found for the strengthening of lattice dislocations (basal slip in hcp Mg, and slip in fcc Al), and these features are reflected in the analytic result of Equation 2. The magnitude of the

strengthening is moderate; at a few % solute concentration, the CRSS is on the order of 10 MPa, which is generally smaller than the CRSS for prism slip and expected values for $\langle c \rangle$ and/or $\langle c + a \rangle$ slip modes. Thus, the solute strengthening of twinning increases the plastic anisotropy between basal and twinning, while only slightly decreasing the plastic anisotropy between twinning and other harder modes of deformation.

We now discuss our results with respect to available experimental data. Twinning in pure single-crystal Mg was studied by Kelly and Hosford [21], who obtained a strength of 3 MPa at room temperature; this value represents the "Peierls stress" for twinning and this value must be added to our prediction of the solute contributions to strengthening to make any comparison with experiments. Direct and systematic experiments measuring the strengthening effect of solutes on twinning in Mg alloys have not been reported. However, there is significant stress-strain data on textured polycrystals with either controlled solute concentrations or commercial compositions, and these studies have been used to estimate the stresses needed to drive twinning. Estimates of the CRSS required for twin growth in Mg AZ31 alloys (2.7 at.% and 0.3 at.%) are reported to be in the range of 6-14 MPa by performing loading-unloading tests [22]. An average of 10 MPa for the CRSS has been reported through twin aspect ratio measurements [23]. Our analysis is readily generalized to predict the yield stress in a multicomponent alloy (Appendix B) and applying the model to Mg AZ31 we predict the total strength (solutes plus Peierls barrier) to be $\tau_y = 14$ MPa at $T = 300K$ and a strain rate of $\dot{\epsilon} = 10^{-3}\text{s}^{-1}$ which was used in the experiments; this is in good agreement with the experimental estimates in [22] and [23]. Stanford and Barnett [24] studied the solute strengthening of various deformation modes in binary Mg-Zn polycrystals and found that the CRSS for twinning is independent of Zn concentration up to 1 at% (2.8 wt%); this is in some disagreement with our prediction that the strength should increase from the Peierls stress of 3 MPa to $\approx$ 8 MPa at 1 at% Zn. On the other hand, in spite of different apparent scalings with concentration, the predicted ratio of twin/basal CRSS $\tau_{\text{twin}}/\tau_{\text{basal}}$ is in excellent agreement with [24] as shown in Figure 6. Note that, the experimental reports of Peierls stress for basal slip is in the range of 1-1.5 MPa. We added an average value of 1.2 MPa to the theoretical solute strengthening predictions. In addition, Ref [24] contains an analysis of previous experimental data for AZ31 [25–28], AZ61 and AZ80 [26]. We extracted the twinning yield stress for these alloys by extrapolating the data to a (large) grain size of 100 μm and applying the appropriate Schmid factor (m = 0.37)

from Figure 10.b of [24]. These experimental values are compared to our predictions for the total twin yield stress (CRSS) including the Peierls barrier in Table II. Given the fact that these experiments are preformed on polycrystals, from which the CRSS must be deduced by correcting for Hall-Petch effects and texture effects, we consider the agreement between prediction and these experiments to be very good. In general, the sources of uncertainty in our predictions are threefold. First, the value of Γ is only from a (good) EAM potential but our results scaling only as $\sqrt{(\Gamma)}$ so quantitative effects are small. Second, the value of $E_{tot}/(Lc^{2/3}))$ is not exactly constant versus w, but the variations are again small. Third, using estimated values for the solute/twin interaction energies leads to small (10%) errors in $E_{tot}/(Lc^{2/3}))$. These uncertainties are thus expected to have minimal effects on the quality of our predictions relative to the experiments.

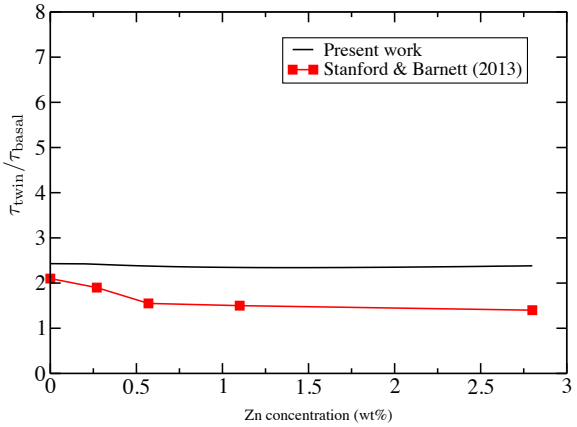

FIG. 6: Ratio of twinning to basal yield stresses (CRSS) as a function of Zn concentration, as predicted by the current model and as measured experimentally.

TABLE II: Twinning yield stress in (MPa) for commercial Mg alloys, as measured and as predicted by the present model. The compositions used in the theoretical model are also presented.

Alloy	c (at%)	Ref. [24]	Present work
AZ31	Al:2.7, Zn:0.37	18	14
AZ61	Al:5.47, Zn:0.37	22	23
AZ80	Al:7.28, Zn:0.187	33	28

Overall, the theory cannot resolve the discrepancies between two different experiments.

Barnett *et al.* [24] conclude that there is no solute strengthening for low Zn concentrations, and attribute the strengthening found by Bohlen *et al.* [26] to the possible presence of precipitates in the commercial alloys. Our present model considers only solute strengthening yet agrees well with the CRSS values deduced from the Bohlen et al. [26] data. Thus, the present theory suggests that precipitate strengthening in the commerical alloys is not present to any appreciable degree. However, we are unable to obtain close agreement with the entirely different results of Barnett et al [24]. The issue of strengthening of twinning by solutes will be resolved experimentally only through designed tests on single-crystal Mg alloys, although such studies may also be complicated by the need to nucleate twins.

V. CONCLUSION

We have computed the structure and solute interaction energies of the $(10\bar{1}2)$ twinning dislocation in Mg by first-principles methods. We have proposed and validated a scaling concept that can be used to estimate solute/twin dislocation interaction energies for other solutes. We have used the solute/twin-dislocation interaction energies as input to a Labusch-type solute strengthening models previously used with success for Mg-Al and Zn basal slip. Due to the small twin dislocation burgers vector and the presence of the adjacent twin boundaries, new feature unique to twins emerge from the theory. In particular, the theory predicts that twin dislocations can have a range of roughening amplitude, and that the strengthening at a given temperature and strain rate is controlled by the roughening amplitude with the highest barrier (maximum stress). Incorporating this feature, we have developed an analytic model of the strength as a function of the solute/twin-dislocation interaction energies and all other materials parameters. The model predicts a larger strengthening of twinning as compared to basal slip at room temperature and various solute concentrations, and the predcited ratio of twin/basal strengthening agrees with experimental observations in [24]. We predict solute strengthening of twin growth of ≈ 14 MPa in AZ31 alloy, consistent with experiments in [22] and [23], and our predictions for strengthening in other commercial Mg-Al-Zn alloys are in good agreement with experiments. We do not address twin nucleation in this paper. In forthcoming work, we will show, however, that twin growth (thickening) is possible starting from a microscopic twin nucleus and that the stresses needed to control twin growth (thickening) and twin strain accumulation are controlled by the solute strengthening

model developed here. Broadly speaking, the present work continues an emerging theme in the field of computational metallurgy in which the development of mechanistic models for strengthening coupled with first-principles based input for crucial chemically-specific energetics of the problem yields quantitative and predictive models of alloying effects on various deformation modes in Mg.

VI. ACKNOWLEDGMENTS

We acknowledge the support of this work by the NSF-GOALI grant number 1309687 and in part by the General Motors/Brown Collaborative Laboratory for Computational Materials Research. Computational resources were provided through General Motors Global Research and Development and by Brown University Center for Computation and Visualization. W.A.C. acknowledges support for this work through a European Research Council Advanced Grant, "Predictive Computational Metallurgy", ERC Grant agreement No. 339081 - PreCoMet.

[1] J. A. Yasi, L. G. Hector Jr, and D. R. Trinkle, Acta Mater **58**, 5704 (2010).

[2] G. P. M. Leyson, L. G. Hector Jr, and W. A. Curtin, Acta Mater **60**, 5197 (2012).

[3] J. A. Yasi, L. G. Hector Jr, and D. R. Trinkle, Acta Mater **59**, 5652 (2011).

[4] J. A. Yasi, L. G. Hector Jr, and D. R. Trinkle, Acta Mater **60**, 2350 (2012).

[5] M. Yoo, J. Morris, K. Ho, and S. Agnew, Metall. Mater. Trans. A **33**, 813 (2002).

[6] G. Kresse and J. Hafner, Phys. Rev. B **47**, 558 (1993).

[7] G. Kresse and J. Furthmuller, Phys. Rev. B **54**, 11169 (1996).

[8] J. P. Pedrew and Y. Wang, Phys. Rev. B **45**, 13244 (1992).

[9] J. F. Nie, Y. M. Zhu, J. Z. Liu, and X. Y. Fang, Science **340**, 957 (2013).

[10] M. H. F. Vannarat, S. Sluiter and Y. Kawazoe, Phys rev B **64**, 224203 (2001).

[11] N. Thompson and D. J. Millard, Phil. Mag. **43**, 422 (1952).

[12] A. Serra, D. J. Bacon, and R. C. Pond, Acta Metall. **36**, 3183 (1988).

[13] A. Serra, D. J. Bacon, and R. C. Pond, Acta Metall. **47**, 1425 (1999).

[14] S. Mendelson, Journal of Applied Physics **41**, 1893 (1970).

[15] G. P. M. Leyson and W. A. Curtin, Phil. Mag. , 5197 (2012).

[16] G. P. M. Leyson, L. G. Hector Jr, W. A. Curtin, and C. F. Woodward, Nature Materials **9**, 750 (2010).

[17] R. Labusch, Physica Status Solidi B **41**, 659 (1970).

[18] X.-Y. Liu, A. J. B, E. Furio, and M. J. A., Modelling Simul. Mater. Sci. Eng **4**, 293 (1996).

[19] M. Ghazisaeidi and W. A. Curtin, Modelling Simul. Mater. Sci. Eng. **21**, 055007 (2013).

[20] G. P. M. Leyson, L. G. Hector Jr, and W. A. Curtin, Acta Mater **60**, 3873 (2012).

[21] E. W. Kelly and W. F. Hosford Jr, Trans. AIME **242**, 5 (1968).

[22] M. R. Barnett, M. Setty, and F. Siska, Metall. Mater. Trans. A **44A**, 2962 (2013).

[23] M. R. Barnett, M. D. Nave, and A. Ghaderi, Acta Mater **60**, 1433 (2012).

[24] N. Stanford and M. R. Barnett, Int. J. Plasticity **47**, 165 (2013).

[25] M. R. Barnett, Z. Keshavarz, A. G. Beer, and D. Atwell, Acta Mater **52**, 5093 (2004).

[26] J. Bohlen et al., Mater. Sci. Eng. A. **462**, 302 (2007).

[27] L. L. Chang, Y. N. Wang, X. Zhao, and M. Qi, Mater. Char. **60**, 991 (2009).

[28] D. L. Yin, J. T. Wang, J. Q. Liu, and X. Zhao, J. Ally. Comp. **478**, 789 (2009).

Appendix A: Construction of the twinning dislocation geometry

Figure 7 shows the process of building the twinning dislocation geometry. We start with a dislocation-free, coherent twin boundary as shown in Figure 7a. The right half of the initial geometry is then shifted in Figure 7b by the corresponding translation vectors $\vec{t}^{\lambda}$ and $\vec{t}^{\mu}$ on each side of the twin boundary. This process creates a step while breaking the coherency at the shifted boundary. To restore the coherent boundary structure, a dislocation with Burger's vector $\vec{b}_t = \vec{t}^{\lambda} - \vec{t}^{\mu}$ is introduced and the final twinning dislocation geometry is shown in Figure 7c . This defect has both dislocation and step characters. Note that Figure 7 is schematic and the translation vectors are exaggerated to highlight the Burger's vector. In practice, $\vec{b}_t$=0.49Å which is very small compared to Mg lattice parameter a_0=3.193Å. Glide of the twinning dislocation along the twin plane results in twin growth.

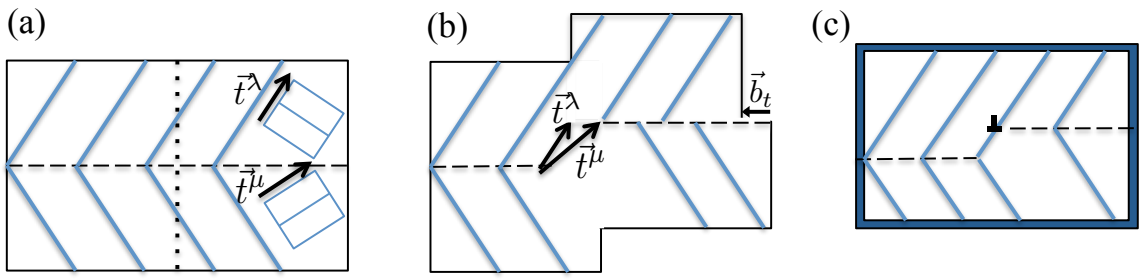

FIG. 7: Schematic of steps required for construction of the twinning dislocation geometry. (a) a dislocation-free, coherent twin boundary with solid blue lines showing the direction of basal planes, and outlines of an hcp cell are shown in the top and bottom lattices along with the translation vectors $\vec{t}^{\lambda}$ and $\vec{t}^{\mu}$. (The right half of initial geometry is shifted in (b) by the corresponding translation vectors at each side of the twin boundary. This process creates a step while breaking the coherency at the shifted boundary. To restore the coherent boundary structure, a dislocation with Burger's vector $\vec{b}_t = \vec{t}^{\lambda} - \vec{t}^{\mu}$ should be introduced. (c) shows the geometry after introducing the dislocation giving a defect with both dislocation and step characters. This twinning dislocation geometry is then relaxed while fixing the atomic positions near the edges of the box shown by solid blue walls.

Appendix B: Analytical calculation of $\tau(T, \dot{\epsilon})$

In the Labusch strengthening model modified by Leyson *et al.*, the total energy from Equation 2 is first optimized with respect to the segment length ζ, yielding the characteristic segment length

$$\zeta_c = \left(\frac{4a_0 w^4 \Gamma^2}{c\Delta\tilde{E}_p^2(w)}\right)^{1/3}.$$

Substituting the above equation in Equation 2 gives the total energy change

$$E_{tot} = -\frac{3}{8\times 2^{1/3}}\left(\frac{c^2\Delta\tilde{E}_p^4(w)}{a_0^2 w^2\Gamma}\right)^{1/3} L \tag{B1}$$

as a function of w only. We note that for the twinning dislocation, $E_{tot}/(c^{2/3}L)$ is nearly constant at various values of the roughening amplitude as shown in Figure 3. We define

$$E_n = -E_{tot}/(c^{2/3}L)$$

which is a positive constant. Rearranging Equation B1 yields:

$$\Delta\tilde{E}_p(w) = \frac{2^{5/2}}{3^{3/4}} a_0^{1/2} w^{1/2}\Gamma^{1/4} E_n^{3/4}. \tag{B2}$$

Next, we substitute the above equation in Equation 4 and Equation 5 to write the energy barrier ΔE_b and zero temperature yield stress τ_{y0} in terms of the constant E_n as follows:

$$\Delta E_b = \frac{4\sqrt{2}-1}{\sqrt{3}}\sqrt{\Gamma E_n} w c^{1/3} \tag{B3}$$

and

$$\tau_{y0} = \frac{\pi 4\sqrt{2}-1}{3b}\frac{E_n c^{2/3}}{w}. \tag{B4}$$

Substituting Equation B3 and Equation B4 into Equation 7 and optimizing with respect to w yields the critical roughening amplitude

$$w_c = \frac{5\sqrt{5}}{12\sqrt{2}-3}\frac{k_B T \log \dot{\epsilon}_0/\dot{\epsilon}}{c^{1/3}\sqrt{\Gamma E_n}} \tag{B5}$$

and $\tau_y(T,\dot{\epsilon})$ evaluated at this amplitude

$$\tau_y(T,\dot{\epsilon}) = \frac{2\pi(33-8\sqrt{2})}{25\sqrt{5}b}\frac{E_n^{3/2}\sqrt{\Gamma}c}{k_B T \ln \dot{\epsilon}_0/\dot{\epsilon}}. \tag{B6}$$

Moreover, this model can be generalized to cases with more than one solute. The above analysis then applies with $c\Delta\tilde{E}_p^2(w)$ replaced by $\sum_i c_i \Delta\tilde{E}_p^{(i)2}(w)$ where i ranges over the number of components. Equation 4 is then rewritten as

$$\Delta E_b^3 = \alpha^3 (\frac{\Gamma w^2}{a_0}) \sum_i c_i \Delta\tilde{E}_p^{(i)2}(w).$$

On the other hand, $\Delta\tilde{E}_p^{(i)}(w)$ are obtained from Equation B2. Therefore, the effective energy barrier for the alloy will be given by

$$\Delta E_b = \frac{4\sqrt{2}-1}{\sqrt{3}}\sqrt{\Gamma} w \left[\sum_i c_i E_n^{(i)3/2}\right]^{1/3}.$$

Similarly

$$\tau_{y0} = \frac{\pi 4\sqrt{2}-1}{3b}\frac{\left[\sum_i c_i E_n^{(i)3/2}\right]^{2/3}}{w}$$

and

$$\tau_y(T,\dot{\epsilon}) = \frac{2\pi(33-8\sqrt{2})}{25\sqrt{5}b}\frac{\sqrt{\Gamma}\sum_i c_i E_n^{(i)3/2}}{K_b T \ln \dot{\epsilon}_0/\dot{\epsilon}} \tag{B7}$$